The Multiscale Impacts of Organized Convection in Global 2D cloud-resolving Models

N. D. Brenowitz[1], A. J. Majda[2,3], and Q. Yang [2,3]

[1]Department of Atmospheric Sciences, University of Washington
[2]Center for Atmosphere-Ocean Science, Courant Institute of Mathematical Sciences, New York University
[3]Center for Prototype Climate Modeling, New York University Abu Dhabi

Key Points:

- 2D cloud resolving models reveal the mechanisms behind multiscale organized convection.
- Low-pass filters can separate spatial scales and quantify dominant feedback mechanisms.
- Mesoscale eddy-momentum transfer can organize planetary-scale convection even without diabatic feedbacks.

Corresponding author: Noah Brenowitz, nbren12@atmos.uw.edu

Abstract

This paper studies the mechanisms behind the multiscale organization of tropical moist convection using a trio of cloud-resolving atmospheric simulations performed in a periodic two-dimensional 32000 km domain. A simulation with interactive surface fluxes and long-wave radiation over a constant sea surface temperature of 300.15 K produces a planetary-scale self-aggregated patch of convection after 80 days of simulation. Fixing the surface fluxes and radiative cooling at a constant value suppresses this planetary-scale organization. However, increasing the stability at the tropopause by adding stratospheric heating produces a simulation which generates a planetary-scale wave after just 30 days. This planetary-scale wave modulates eastward-propagating synoptic-scale waves which in turn modulate westward-propagating mesoscale convective systems (MCS).

Low-pass filters are used to diagnose the feedbacks which produce large-scale variance of zonal velocity, buoyancy, and humidity. The planetary-scale buoyancy variance and zonal velocity variance are related to the available potential energy (APE) and kinetic energy (KE) budgets, respectively. In the simulation with stratospheric heating, planetary-scale KE is created by vertical advection, converted to APE, and then dissipated by latent heating, mixing, and other buoyancy sources. Without stratospheric heating, any KE produced by vertical advection feedbacks is immediately damped in the stratosphere. The mesoscale eddy-flux convergence of zonal momentum dominates the total vertical advection feedback on the planetary-scale KE, and its vertical structure is consistent with the westward-propagating MCSs. Overall, these results demonstrate that multiscale feedbacks can organize deep convection on planetary scales even when surface fluxes and radiation are constant.

1 Introduction

Moist atmospheric convection in the tropics is organized in a hierarchy of spatial and temporal scales. Convective systems range in scale from a single cumulus cloud, to mesoscale convective systems (MCSs) [*Houze*, 2004], to convectively coupled equatorial waves (CCEWs) on the synoptic-scale [*Kiladis et al.*, 2009], and, finally, to planetary/intraseasonal oscillations such as the Madden-Julian Oscillation [*Madden and Julian*, 1971, 1972; *Zhang*, 2005]. For example, *Nakazawa* [1988] showed an eastward-propagating supercluster with westward-propagating mesoscale disturbances embedded inside. *Chen et al.* [1996] observed several westward-propagating superclusters over the western Pacific during the active phase of the MJO. In turn, these superclusters contained mesoscale disturbances of tropical convection that moved in various directions. *Moncrieff et al.* [2017] found that tropical waves of various scales are embedded in the planetary-scale convective envelope of an MJO observed during the Year of Tropical Convection (YOTC) virtual global field campaign. Convective systems on all these scales often exhibits a self-similar vertical structure that tilts up and towards the rear [*Mapes et al.*, 2006; *Majda*, 2007]. This self-similarity probably owes to the predominance of three cloud types in tropical convection—shallow congestus, deep, and stratiform—which *Johnson et al.* [1999] found based on analyses of shipboard radar data from Tropical Ocean Global Atmosphere Coupled Ocean-Atmosphere Response Experiment (TOGA-COARE). *Mapes et al.* [2006] concluded that an MCS may be a small analog or prototype of larger scale waves by hypothesizing a multiscale structure. The multicloud models mimic these features [*Khouider and Majda*, 2006, 2008] and lead to significantly improved realistic variability in the MJO and monsoon in operational models [*Goswami et al.*, 2017a,b]. A successful theory for realistic convective organization should also account for these observational characteristics.

In recent years, the cloud-resolving models (CRM) have become powerful and practical tools for simulating organized tropical convection. CRMs simulate the non-hydrostatic dynamics of the atmosphere with horizontal resolutions of around 1 km to 4 km, and, therefore, do not need to parameterize deep cumulus convection. These improvements owe to both increased computational resources and progress in numerical methods and the representation of physical processes [*Prein et al.*, 2015; *Khain et al.*, 2015]. In an early study, *Grabowski and Moncrieff* [2001] demonstrated that a CRM over a uniform sea surface temperature (SST) can reproduce multiscale organized convection in a 2D periodic domain with a size of 20 000 km. Their simulation contained many eastward-propagating synoptic-scale CCEWs, each of which contained numerous westward-propagating MCSs. Also, 2D CRMs performed in large domains over non-uniform SST can generate realistic planetary-scale circulations and intra-seasonal variability [*Slawinska et al.*, 2014]. Overall, 2D simulations are a computationally cheap method for performing a simulation in a domain that is large enough to contain the dominant scales present in observations.

Three dimensional (3D) CRM simulations are computationally expensive, so many studies focus on radiative convective equilibrium (RCE) in limited area domains. RCE experiments study the evolution of moist-convective dynamics without any prescribed forcing [*Held et al.*, 1993; *Bretherton et al.*, 2005], and are usually performed in the absence of rotation. However, rotating RCE simulations are useful framework for studying tropical cyclone dynamics [*Khairoutdinov and Emanuel*, 2013]. In the absence of rotation, these limited area RCE experiments develop a form of convective organization known as self-aggregation when the domain size is larger than about 200 km [*Bretherton et al.*, 2005; *Muller and Held*, 2012]. Self-aggregation occurs when disorganized clouds coalesce into a single dominant patch of convection. It can occur in 2D domains [*Held et al.*, 1993; *Yang*, 2017] as well as 3D domains of different horizontal aspect ratios [*Wing and Cronin*, 2016].

Notably, *Bretherton et al.* [2005] found that self-aggregation at RCE requires spatial inhomogeneities in the radiation heating/cooling and surface heat fluxes. *Wing and Emanuel* [2014] further quantified these diabatic feedback mechanisms using the budget for the zonal variance of column-integrated moist static energy. *Bretherton and Khairoutdinov* [2015] then used this framework to quantify the strength of these feedbacks in a near-global aqua-planet simulation with ambient rotation and realistic circulation. They found that surface fluxes tend to suppress aggregation, but radiative processes tend to aggregate convection with a time scale of 10 d.

While convective aggregation is well studied, it is unclear how relevant it is to realistic atmospheric flows. The real atmosphere rotates and often has significant wind shear, and [*Held et al.*, 1993] only saw aggregation after constraining the domain-mean wind to vanish, and *Bretherton and Khairoutdinov* [2015] noted that radiative feedbacks are only strong enough to act on the largest spatial and slowest time scales. Also, these previous studies focused column-integrated moist static energy budgets, an analysis which naturally emphasizes the importance of thermodynamics compared to kinematics and surface fluxes compared to internal processes.

Another body of work highlights the dynamical interactions that organize moist convection on large-scales. *Majda and Stechmann* [2009] developed the so-called skeleton model for the MJO, which is based on interactions between moisture, convective activity and equatorial fluid dynamics. They point out that beyond the MJO's skeleton, the MJO's "muscle" includes fine vertical structure and up-scale momentum transport from sub-planetary convection and waves. Along these lines, theoretical models focusing on the nonlinear interactions across scales have been developed based on rigorous multiscale asymptotic analysis[*Majda and Klein*, 2003; *Majda*, 2007]. Essentially, multiscale models predict that there are three types of nonlinear interactions across scales. First, eddy-flux convergences of momentum and temperature from smaller scales accumulate in time and drive waves on larger scales. Second, the large-scale velocity advects the small-scale quantities. Third, the flux of the larger-scale quantities by the small-scale velocity appears in the small-scale budgets in some multiscale models [*Biello et al.*, 2010]. Thus, multiscale models describe an alternative mechanism than diabatic feedbacks for the large-scale organization of tropical convection. These multiscale models highlight the central role of vertically-tilted synoptic-scale anomalies [*Majda and Biello*, 2004; *Biello and Majda*, 2005, 2006] and the up-scale impact of the diurnal cycle through eddy flux divergence of temperature [*Yang and Majda*, 2014; *Majda and Yang*, 2016]. In so doing, they can explain many of the observed characteristics of the MJO.

The main goal of this paper is to show that multiscale feedbacks can organize tropical moist convection in a cloud-resolving model on planetary-scales even with homogeneous surface fluxes and radiative forcing. To do this, we perform CRM experiments similar to those of *Grabowski and Moncrieff* [2001] in a 2D domain that is 32 000 km in length. Unlike most self-aggregation studies, these experiments are forced with a barotropic easterly wind. A simulation with homogeneous surface fluxes and fixed radiative cooling in the troposphere and heating in the stratosphere quickly develops a planetary-scale wave with multiscale organization. We then develop a technique to decompose the model outputs into planetary-, synoptic-, and meso-scale components, and use this to define budgets for the variance of each scale. Special attention is paid to the planetary-scale variance budgets of the velocity, buoyancy, and moisture. The former two are closely related to the kinetic energy (KE) and available potential energy (APE). In the run with the planetary-scale wave, we find that the vertical eddy-momentum flux from mesoscales is the dominant source of planetary-scale total energy. Finally, we show that the vertical and horizontal structure of these eddy-fluxes and the planetary-scale fields is consistent with the multiscale theories.

Section 2 describes the configuration of the 2D CRM experiments. Then, Section 3 summarizes the basic climatology and variability of the simulations. In Section 4 we introduce an automatic method to decompose the model outputs and the budget equations into different scales, and Section 5 uses this framework to derive planetary and synoptic-scale budgets for the KE, APE, and humidity variance. Finally, the multiscale feedbacks are discussed in Section 6. First, we decompose the vertical advection into triad interactions between scales and show the time average feedbacks in Section 6.1. Next, Section 6.2 shows the vertical structure of the up-scale eddy-flux convergences and the corresponding planetary-scale fields. We conclude in Section 7.

2 Model Configuration

Two dimensional (2D) simulations using cloud-resolving models can reproduce many interesting aspects of multiscale tropical flows while remaining computationally inexpensive. For instance, *Grabowski and Moncrieff* [2001] produced synoptic-scale convectively coupled waves (CCWs) in a 20 000 km zonal domain without any rotation. This setup mirrors the structure of the atmosphere at the equator, and is large enough to permit multiscale processes, unlike limited area 3D simulations. Since this paper focuses on multiscale processes rather than realistic 3D dynamics, we aim to reproduce the 2D simulations of *Grabowski and Moncrieff* [2001] as closely as possible.

We use the Version 6.9 of the System for Atmospheric Modeling (SAM), which is a popular model for studying clouds and convective processes [*Khairoutdinov and Randall*, 2003]. SAM is an excellent model for this study because it solves the anelastic version of the equations of motions in idealized geometries, which allows easy configuration and fast execution. For more details on using the anelastic approximations, we refer the reader to *Pauluis* [2008]. Many studies have used this model to study convective self-aggregation in limited area [*Bretherton et al.*, 2005; *Wing and Emanuel*, 2014] and near-global domains [*Bretherton and Khairoutdinov*, 2015; *Wing and Cronin*, 2016]. Therefore, we will also use a SAM in a planetary-scale configuration to study the processes underpinning convective organization.

We run SAM in three different configurations to reveal different archetypes of convective organization. First, a control experiment is intended to recreate the setup of *Grabowski and Moncrieff* [2001]. The simulation is performed on a periodic horizontal domain which is $2^{15} = 32\,768$ km in extent with a horizontal grid spacing of 2 km. The vertical grid has 34 levels between 0 m and 27 000 m, with a spacing varying smoothly from 50 m near the surface to 1200 m in the mid-troposphere. At the top of the domain, a sponge layer damps the velocity and thermodynamic fields towards the initial profile. Each experiment uses one-moment microphysics and a Smagorinsky sub-grid-scale turbulence scheme. With a time step 5 s, 100 days of output can be generated in about 24 hour on single machine with 20 processors, so that we can cheaply investigate the mechanisms that organize tropical flows on intraseasonal time scales and planetary length scales.

Like *Grabowski and Moncrieff* [2001], the zonal winds are damped towards a $10\,\mathrm{m\,s^{-1}}$ barotropic easterly wind with a 1 d time scale, which induces a mean easterly flow. This flow is largest around 800 hPa and smallest near the surface (cf. Figure 1), so that there is significant vertical wind shear in the lower atmosphere. This strong wind shear and mean easterly zonal flow is the biggest difference between our simulations and those performed in the self-aggregation studies cited in the introduction.

To compare and contrast the mechanisms that organize convection a variety of scales, we perform three experiments with different diabatic forcings. We first perform an experiment over a uniform 300.15 K sea surface temperature (SST) with fully interactive long-wave radiation and surface fluxes, but no shortwave radiation or diurnal cycle. This simulation will henceforth be abbreviated by LW. This setup has the most similar diabatic forcing to studies like *Wing and Emanuel* [2014]. However, it is not clear that diabatic feedbacks are the dominant organization mechanism in a realistic atmosphere, so we also perform a control simulation with constant surface fluxes and

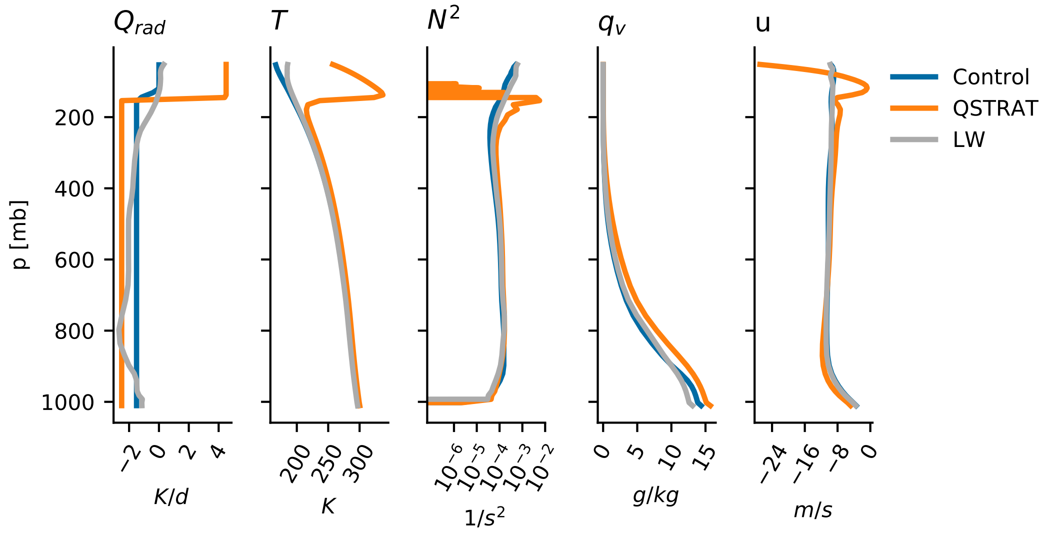

Figure 1. Zonal-mean climatology for the Control, QSTRAT, and LW simulations. The averages are taken over the final 60 days of simulation to allow for a 40 day equilibration time. The stratification (N^2) near 200 hPa is much larger than in the QSTRAT run the other two simulations. The stratification is plotted with a logarithmic horizontal axis.

radiative cooling. *Bretherton et al.* [2005] note that this will suppress convective self-aggregation in limited area domains. The sensible and latent heat fluxes are fixed at 210.6 W m^{-2} and 31.20 W m^{-2}, respectively, and we impose a uniform radiative cooling of 1.5 K d^{-1} below 150 hPa. Most of the dissipation in the control run occurs in the stratospheric sponge layer of the control simulation, which can have a profound effect on convective organization. To reduce this dissipation, we perform one final simulation—henceforth abbreviated by QSTRAT—with a constant stratospheric heating of 4.5 K d^{-1} above 150 hPa. We increase the cooling rate below this level to 2.5 K d^{-1} to ensure that the mass-weighted vertical integral of radiative tendency equals that of the Control run. While these three simulations may not be realistic, they do plausibly illustrate the different mechanisms which give rise to organization on various spatial and temporal scales.

3 Basic Results

Figure 1 shows the equilibrium vertical profiles for several model variables. We compute these profiles by averaging zonally and temporally over the final 60 days of the model simulation. The radiative heating for the Control and QSTRAT simulations simply show the imposed forcing we describe above. The heating in the LW simulations is fairly similar to the Control simulation, with cooling in the troposphere and no heating above 150 hPa, and all the other plotted quantities have a

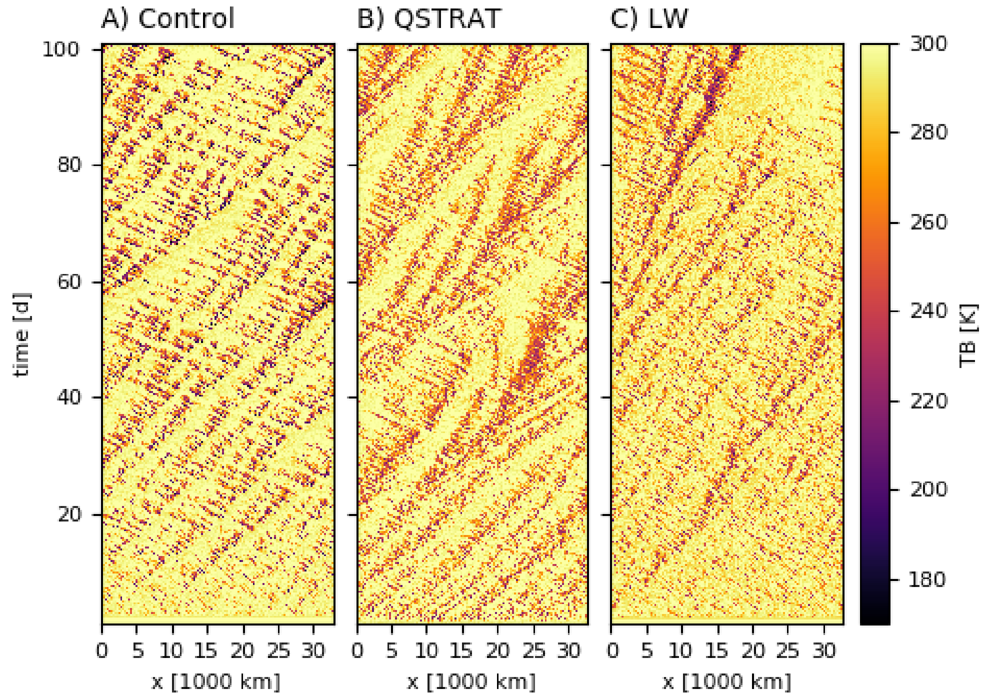

185 **Figure 2.** Hovmoller diagrams of brightness temperature (TB) for the Control (A), QSTRAT (B), and LW
186 (C) simulations.

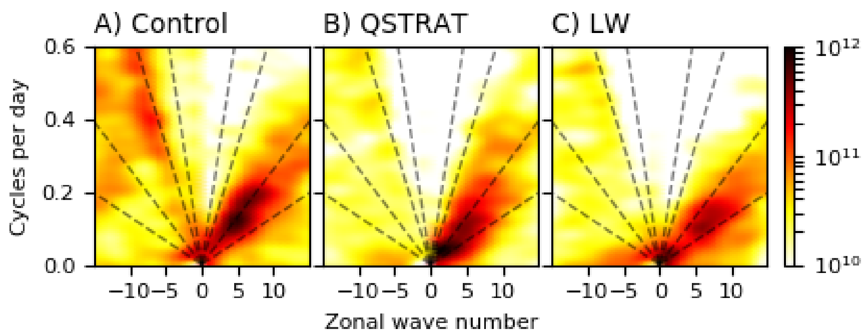

187 **Figure 3.** Space-time power spectra of TB for the three simulations show in Figure 2. The dashed black lines
188 indicate wave speeds of 5, 10, 25 and 50 m s^{-1}.

very similar structure between the Control and LW simulations. On the other hand, the stratospheric heating in QSTRAT induces a near discontinuity in the temperature field at 150 hPa, which appears as a spike of stability (N^2) there. Apart from this, the QSTRAT run is slightly warmer and moister than the other two simulations. The very large stability at 150 hPa acts as a rigid lid, which traps the interesting dynamics below that level. Finally, the three simulations have similar wind profiles below 150 hPa, with strong wind shear below 800 hPa. Overall, the most important difference between the simulations is the rigid lid in the QSTRAT run.

Figure 2 contains space-time diagrams of brightness temperature (TB), a proxy which indicates high cloud tops and strong precipitation for low temperature. The first twenty days of each simulation consist of westward-propagating MCSs embedded within eastward-propagating synoptic-scale CCEWs. That said, it does appear that the convection is less organized in the first 20 days of the LW simulation than the two runs with fixed diabatic forcing.

Grabowski and Moncrieff [2001, cf. Fig 4] carefully document this mesoscale synoptic-scale structure, and most of the features are the same. These MCSs tilt up and to the east as the propagate to the west. In the sections below, we will show how these mesoscale structures effect the larger scales present in the simulation.

Unlike the mesoscale structures, the simulations all differ in their degree of planetary-scale organization. The control simulation shows no planetary-scale TB pattern, but planetary-scale eastward-propagating disturbances appear after 20 days in the QSTRAT run and continue until the end of simulation. This disturbance has wavenumber two zonal structure and forms the envelope of many synoptic-scale waves which also propagate to the east, a multiscale structure which mirrors that of the synoptic-scale waves. On the other hand, the LW simulation develops a planetary-scale structure at a much slower rate than QSTRAT simulation, and this structure hardly moves with respect to the fixed reference frame. This near-standing convection is similar to the self-aggregated convection, but appears much more slowly, likely due to the strong meso-scale activity.

The wave propagation speeds as well as dominant spatio-temporal scales in these simulations are more obvious in frequency domain as shown in Figure 3. We compute the power spectra by subtracting the domain and time mean, and then taking the fast Fourier transform of the 100 day time series. We then smooth the spectra using a Gaussian kernel with a standard deviation of 1.5 wave numbers in the wavenumber and $(100\,\mathrm{d})^{-1}$ in the frequency direction. *Wheeler and Kiladis* [1999] use a similar technique for smoothing their spectra. The Control simulation has a large eastward peak around wavenumber 5 corresponding to the eastward-propagating synoptic-scale waves. In the

QSTRAT run, this eastward peak shifts towards smaller wavenumber and lower-frequencies, which is the spectral signature of the planetary-scale oscillation seen in Figure 2. In the LW simulation, the eastward waves are weaker and move at a slower speed. The Control simulation has much more westward power at high frequencies than the LW or QSTRAT simulations do. That notwithstanding, Figure 2 shows obvious westward streaks in TB for these last two simulations. Overall, the spectra shown in Figure 3 mirror the obvious features seen in the Hovmoller diagrams shown in Figure 2.

The results in this section show that the Control runs does not have any planetary-scale organization, while the QSTRAT and LW runs do. The main difference between the LW and Control run is that the former has interactive radiation and surface fluxes. These feedbacks likely explain the planetary-scale organization in the LW simulation, a fact documented in many studies (e.g. *Wing and Emanuel* [2014]). Moreover, the fact that the pattern does not appear in the LW simulation for 80 days is consistent with evidence that self-aggregation feedbacks act slowly in environments with nonzero mean winds *Bretherton and Khairoutdinov* [2015]. Because these diabatic feedbacks are absent in the QSTRAT simulation, which has uniform heating and surface fluxes, the stratospheric heating and stability increase near the tropopause must somehow cause this disturbance. The obvious three-scale structure of the QSTRAT hints that multiscale interactions could be important. Thus, we hypothesize that nonlinear interactions between scales can create planetary-scale convective organization even in the absence of diabatic feedbacks.

4 Multiscale Decomposition

4.1 Filter based multiscale decomposition

We now describe a method to decompose the model outputs into meso-, synoptic-, and planetary-scale components. The theoretical asymptotic models described above assume that the length of the mesoscale (synoptic scale) is infinitesimally smaller than the length of the synoptic (planetary) scale. Unfortunately, neither the spectra of our simulations (cf. Figure 3) nor that of the real atmosphere [*Kiladis et al.*, 2009] support this asymptotic assumption. Nevertheless, it does approximately describe the three-scale structure we observe in the QSTRAT run.

The defining difference between these scales is related to the smoothness of the underlying field, so we use low-pass filters in the zonal direction to separate the scales automatically. We define the low-pass filtered field as the large-scale component, and the residual as the small-scale component. The simple 2D geometry and periodic boundary conditions make it trivial to implement these filters

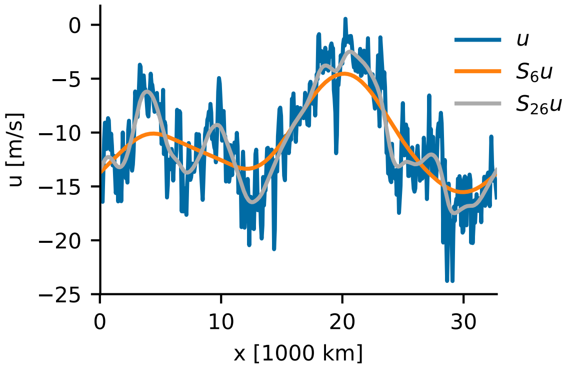

Figure 4. Demonstration of the low-pass filter on the zonal velocity at $z = 3000$ m and $t = 80$ d of the QSTRAT simulation. The original data is shown along with the low-pass filtered results for two different bandwidths.

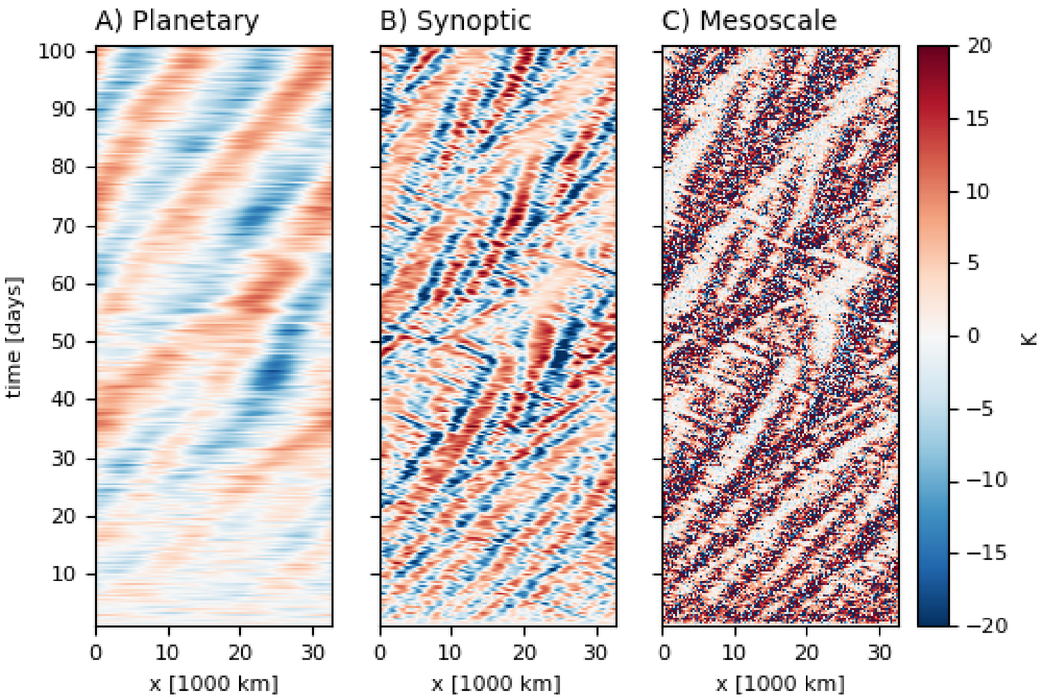

Figure 5. Multiscale decomposition of brightness temperature from the QSTRAT simulation. The three panels show TB^P (A), TB^S (B), and TB^M (C).

in the frequency domain, but *Aluie et al.* [2017] take a similar approach in spherical geometry to analyze scale interactions in ocean turbulence.

After extensive experimentation with low-pass filters based on splines, empirical orthogonal functions, and Gaussian kernels, we ultimately choose a simple filter in the Fourier domain. It is prohibitively expensive to perform the filtering operation on the full data, which has over 16000 horizontal grid points, so we first coarse-grain the input data onto 128 km grid boxes. Then, the filter is defined in the zonal wavenumber domain by

$$s_\alpha[k] = \frac{1}{1 + \alpha |k|^4},$$

so that the filtered version of some field $f(x)$ is given by $S_\alpha f = \mathcal{F}^{-1}[\mathcal{F}[f] \cdot s_\alpha]$, where $\mathcal{F}$ and $\mathcal{F}^{-1}$ are the discrete Fourier transform and its inverse, respectively. Here, S_α is a linear operator which denotes the action of the low-pass filter on $f(x)$. The bandwidth of this filter is controlled by the parameter α, which effectively penalizes the fourth derivative of f

A convenient way to choose α is based on the effective degrees of freedom, which is defined as by $m(\alpha) = \sum_k s_\alpha[k]$. Roughly, the $m(\alpha)$ describes the numbers of degrees of freedom that remain after applying the S_α. For example, If $\alpha = 0$, then the $s_0[k] = 1$, so that $m(0) = n$, where n is the original number of horizontal grid points. As $\alpha \to \infty$, $m(\alpha) \to 1$, which implies that $S_\infty f$ is just the zonal mean of f. Thus, the length scale associated with a $m(\alpha)$ is given by $L/m(\alpha)$, where $L = 32\,768$ km is the length of the overall domain. In practice, the cutoff scale of the filter is controlled by setting an effective numbers of degrees of freedom m^*, and using a nonlinear solver to compute $\alpha^* = m^{-1}(m^*)$. We will, therefore, change our notation slightly so that S_m is the low-pass filter corresponding to m degrees of freedom.

Figure 4 shows the effect of filtering the zonal velocity field at $z = 3$ km with different effective degrees of freedom. The unfiltered velocity shows many spikes and small scale structures. The low-pass filtered velocity with $m = 6$ (i.e. $S_6 u$) only captures the planetary-scale undulations. Next, applying the filter with $m = 26$ captures all the fluctuations with extents larger than a few thousand kilometers. Using this as a guide, we define the planetary- and synoptic-scale components to correspond to $m = 6$ and $m = 26$, respectively.

Just as one filter can separate two physical scales, multiple filters with different bandwidths can decompose the data into three or more scales. Let $f(x)$ be a physical variable which depends on x. The largest "scale" of f is the zonal mean of f, which we denote by

$$\overline{f} = \frac{1}{L} \int_0^L f(x) dx. \tag{1}$$

Then, we define the planetary-scale component by

$$f^P = S_6 f - \bar{f} \tag{2}$$

so that $\overline{f^P} = 0$. Similarly, the synoptic-scale component f^S is given by

$$f^S = S_{26}\left(f - \left[\bar{f} + f^P\right]\right). \tag{3}$$

Finally, the mesoscale component is the residual left after subtracting the domain mean, planetary-scale, and synoptic-scale components from f. Recall that the mesoscale component does not include smaller scale contributions because we initially coarse-grained the the field f onto 128 km boxes. In summary, we can apply several low-pass filters with decreasing bandwidths to to compute the multiscale decomposition given by

$$f = \bar{f} + f^P + f^S + f^M. \tag{4}$$

Figure 5 shows that this procedure can effectively separate the meso-, synoptic, and planetary scales in the QSTRAT simulation. A strong eastward-propagating disturbance appears in the planetary-scale pattern around day 20. Negative anomalies in the planetary-scale panel correspond to regions with enhanced precipitation, and it appears that most of synoptic-scale activity is confined to these regions. Likewise, the mesoscale is most active in the areas with negative synoptic-scale anomalies. Thus, the low-pass filter based decomposition technique provides an automatic way to diagnose the multiscale structures in the QSTRAT run, which we discussed in Section 3.

4.2 Multiscale decomposition of the governing equations

We also use this decomposition technique to decompose the budget equation for a given quantity f, into the three separate scales. In the anelastic framework, the evolution of an arbitrary tracer f is given by

$$\frac{\partial f}{\partial t} + (uf)_x + \frac{1}{\rho_0}(\rho_0 w f)_z = S_f, \tag{5}$$

where $\rho_0(z)$ is the base state density profile and S_f are the other source terms in the budget. For convenience we will denote the horizontal advection terms by $H_f = -(uf)_x$ and the vertical advection terms by $V_f = -\frac{1}{\rho_0}(\rho_0 w f)_z$. Then, taking the planetary-scale component of this equation gives

$$\frac{\partial f^P}{\partial t} = V_f^P + H_f^P + S_f^P \tag{6}$$

where the superscript P denotes the planetary-scale component.

In general, the planetary-scale component of the horizontal advection terms will be small because $(uf)_x^P \propto 1/L_P$ where L_P is the planetary length scale. This fact reflects the results of theoretical multiscale asymptotics. On the other hand, vertical advection terms do not involve a horizontal derivative and may be large.

5 Budget Analyses

5.1 Moisture, Buoyancy, and Momentum Budgets

To identify the important physical mechanism behind the multiscale organization in the QSTRAT run, we analyze the budgets of zonal momentum, buoyancy, and water vapor. For diagnostic purposes, we neglect the virtual effect and approximate the buoyancy by $B = g(\theta - \theta_0)/(\theta_0)$, where θ_0 is the time average of the zonal mean potential temperature over the final 50 days of the simulation. Then, the budgets for the velocity u, the buoyancy B, and the water vapor specific humidity, q, are given by

$$\frac{\partial u}{\partial t} = H_u + V_u - \phi_x + S_u, \tag{7}$$

$$\frac{\partial B}{\partial t} = H_B + V_B - N^2 w \left(1 + \frac{B}{g}\right) + S_B, \tag{8}$$

$$\frac{\partial q}{\partial t} = H_q + V_q + S_q. \tag{9}$$

We estimate the horizontal and vertical advection terms using second order centered finite differences. There are two important linear terms in the these equations. First, the buoyancy budget has a contribution from adiabatic motions given as $N^2 w$. The Brunt-Väisälä frequency is given by $N^2 = g\partial_z \log \theta_0$ where θ_0 is the reference potential temperature profile used to define the buoyancy. In future sections, we will include the small $\frac{B}{g}$ term in the residual terms S_B for simplicity. We approximate the vertical derivative in N^2 using a cubic spline. Second, the zonal momentum is forced by the pressure gradient term $-\phi_x$, which we also approximate using second order centered differences.

We compute the remaining source terms, S_B, S_q, and S_u as a residual from the known terms. The source terms for the buoyancy equation, denoted by S_B, include the effect of latent heating, radiation, and any turbulence or advection occurring on scales smaller than coarse-graining size of 128 km. Likewise, S_q includes condensation and evaporation terms, and S_u includes the effect of turbulence and convective momentum transports occurring below the coarse-graining scale.

5.2 Scalewise variance budgets

Variance budgets can conveniently summarize the relative importance of the terms in the Eqs. 7–9 for different physical scales. In particular, *Wing and Emanuel* [2014] study the variance about the zonal mean of vertically integrated moist static energy (MSE). They identify increased column-MSE variance with convective aggregation, and quantify the magnitude and sign of different terms in the budget. *Bretherton and Khairoutdinov* [2015] use a similar approach to diagnose the column-MSE budget for each wave-number separately.

We could take a similar approach to compute the variance of the column-integrated budget of some variable f at some scale α where $\alpha \in P, S, M$ is a placeholder. First, define the operator given by

$$\langle f \rangle = \int_0^H f \rho_0(z) dz \tag{10}$$

for mass weighted vertical integration. Then, the analogous variance budget to what *Wing and Emanuel* [2014] describe is given by taking a vertical integral of Eq. 6 and then multiplying by $\langle f^\alpha \rangle$ to get

$$\frac{1}{2} \frac{d\overline{\langle f^\alpha \rangle^2}}{dt} = \overline{\langle f^\alpha \rangle \langle V_f^\alpha \rangle} + \overline{\langle f^\alpha \rangle \langle H_f^\alpha \rangle} + \overline{\langle f^\alpha \rangle \langle S_f^\alpha \rangle}. \tag{11}$$

Unfortunately, there are some problems with this approach. First, Eq. 11 cannot reveal any feedback mechanisms involving momentum because the anelastic divergence free condition ensures that $\langle u \rangle$ is constant in space, which implies that $\langle u^P \rangle = \langle u^S \rangle = 0$. Second, studying the zonal variance of vertically integrated quantities can mask the importance of covarying vertical structures such as the tilted convection in CCEWs and propagating MCSs. The way vertical profiles covary is especially important for vertical advection, but $\langle V_f \rangle = \langle \frac{1}{\rho_0} (\rho_0 w f)_z \rangle = \rho_0 w f|_{z=0}$, assuming the flux vanishes at the upper boundary. This means that $\langle V_f \rangle$ is the surface flux of f, which is homogeneous in space in our QSTRAT and Control runs. One could construe this to mean that vertical advection plays no role in convective organization when surface fluxes are constant, but as shown below, it actually does. Thus, column-integrated budgets overemphasize the importance of surface fluxes and thermodynamic quantities like humidity relative to internal processes and kinematic quantities like velocity.

This problem can be fixed by studying the variance budgets of 3D quantities. We quantify the variance of a quantity f on a certain scale $\alpha \in \{P, S, M\}$ by taking a zonal average of $\frac{1}{2}(f^\alpha)^2$. This quantity is called the α-scale variance of f, and an equation for its time evolution can be derived by multiplying Eq. 6 by f^α and taking a zonal average. This is given by

$$\frac{1}{2} \frac{\partial \overline{(f^\alpha)^2}}{\partial t} = \overline{f^\alpha H_f^\alpha} + \overline{f^\alpha V_F^\alpha} + \overline{f^\alpha S_f^\alpha}. \tag{12}$$

This equation is deceptively similar to Eq. 11, but can account for covariance between the vertical structures of field and its source terms. For convenience, we often refer to the quantities on the

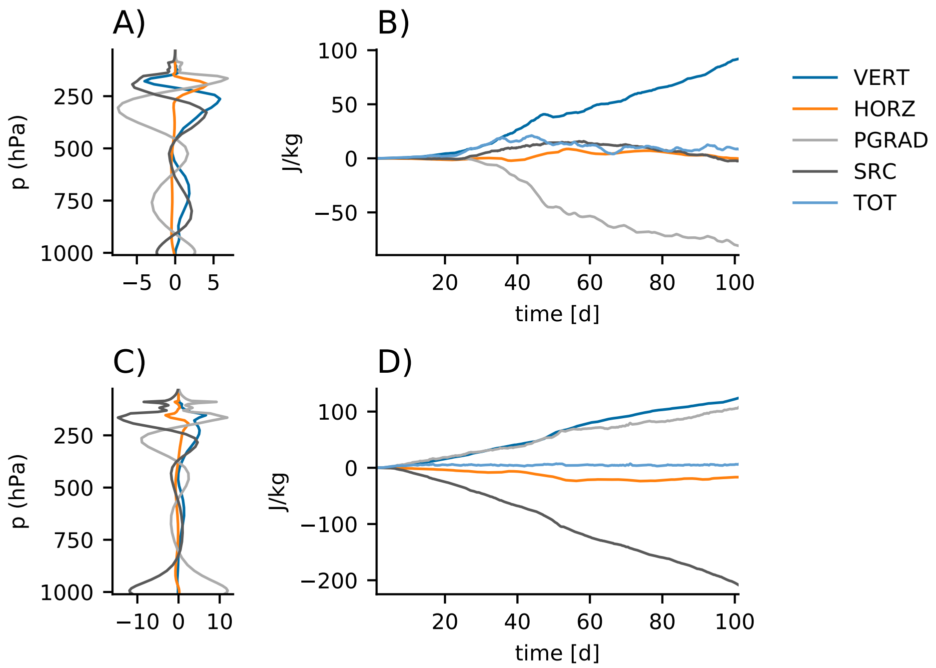

Figure 6. Vertical structures and time variability of the planetary-scale and synoptic-scale KE budgets for the QSTRAT simulation. The planetary and synoptic-scale KE budgets are shown in the first and second rows, respectively. The first column shows the time mean vertical structure of the KE feedbacks for the planetary (A) and synoptic-scales (B). The second column shows the cumulative effective of the mass-weighted average KE feedbacks for the planetary (B) and synoptic (D) scales. The mass weighted average is given by $\langle\cdot\rangle/M$, where $M = \langle 1 \rangle$ is the mass of the atmospheric column. Each panel shows the feedbacks due to vertical advection (VERT), horizontal advection (HORZ), pressure gradients (PGRAD), and the residual source terms (SRC). Panels B and D also show the total planetary and synoptic-scale KE, respectively.

right hand side as *feedbacks*. For example, $\overline{f^{\alpha} H_f^{\alpha}}$ is the feedback due to horizontal advection on the α-scale variance budget of f.

We summarize the impact of the individual feedbacks in Eq. 12 by taking vertical integrals and integrating forward in time. This removes the need to estimate the time derivative term, which allows a less noisy estimate of the residual terms. For all of these quantities, positive (negative) values indicate that a feedback tends to increase (decrease) the variance on the target scale.

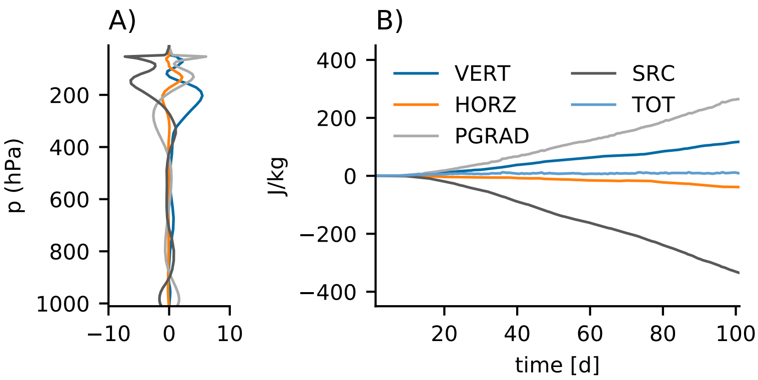

Figure 7. Planetary-scale KE budget for the Control simulation. Same as Figure 6 A and B but for the Control simulation.

5.2.1 Kinetic Energy

The kinetic energy (KE) budgets for the planetary and synoptic scales can reveal the important kinematic feedbacks. The KE for a given scale α is given by

$$\mathrm{KE}^{\alpha} = \overline{\frac{1}{2}(u^{\alpha})^2}. \tag{13}$$

The budget for KE^{α} is obtained from the momentum budget (Eq. 7) in the usual way to give

$$\frac{1}{2}\frac{\partial \mathrm{KE}^{\alpha}}{\partial t} = \overline{u^{\alpha} H_u^{\alpha}} + \overline{u^{\alpha} V_u^{\alpha}} - \overline{u^{\alpha} \phi_x^{\alpha}} + \overline{u^{\alpha} S_u^{\alpha}}. \tag{14}$$

Figure 6 shows the time-mean vertical structure of the feedback terms on the right hand side of Eq. 14 for both the planetary and synoptic-scale ($\alpha = P, S$). It also shows the mass-weighted average for each feedback term integrated forward in time. For example, the cumulative effect of the mass-weighted pressure gradient feedback for the planetary-scale is given by

$$\int_0^t -\langle \overline{u^P \phi_x^P} \rangle dt'.$$

The cumulative effect of the other feedbacks are defined analogously.

Vertical advection of horizontal momentum is the largest positive feedback in the planetary kinetic energy budget. It is balanced by the pressure gradient term, which tends to remove planetary-scale KE, while the sub-grid-scale residual terms and horizontal advection feedbacks are much smaller. These feedbacks have a similar relationship when looking at the detailed vertical structure. The vertical advection feedback is consistently positive throughout the column, and the pressure gradient is mostly negative, and shifted downward slightly. The residual feedbacks are large for some heights even though they have a little vertically integrated effect. Despite being smaller than the cumulative feedbacks, KE^P is quite large, and shows substantial fluctuation over the course of the simulation.

On the other hand, the synoptic-scale KE is much smaller and barely fluctuates in time. In addition, the dominant feedbacks are subtly different. Vertical advection and pressure gradients almost equally amplify the synoptic-scale KE, and the residual term balance this positive feedback. Most of the dissipation due to source terms occurs below 800 hPa and above 400 hPa. Below 800 hPa, the pressure gradient terms balance this sink, whereas vertical advection is the dominant positive feedback above 400 hPa. As before, horizontal advection has little effect.

Figure 7 shows the planetary-scale KE budget for the Control simulation, which does not have a strong planetary-scale signal (cf. Figure 2). The dominant balances in this Control simulation are completely different than for the QSTRAT simulation, which has a planetary-scale oscillation. The residual momentum source had little impact in the QSTRAT run, but it is the largest negative KE feedback in the Control run. Also, the vertical structures of these feedbacks differ between the two simulations. In the control run, the residual terms are consistently negative for most vertical levels, but this feedback is strongest above 300 hPa. In the QSTRAT run, positive residual feedbacks in the mid-troposphere balance the negative feedbacks in the lower and upper atmosphere. Moreover, these residual feedbacks are much smaller in magnitude in the QSTRAT run than the Control run. In turn, pressure gradients generate KE to balance this large sink.

Interestingly, the vertical advection feedback has a similar sign and magnitude in both the QSTRAT and Control runs, which suggests that this process is unchanged between the simulations. This all indicates that in the absence of surface flux or radiative feedbacks, large stratospheric dissipation prevents the formation of a planetary-scale oscillation. Then, reducing this dissipation, as in the QSTRAT run, allows the vertical advection to become the dominant positive feedback, which must be balanced by a negative pressure gradient feedback.

5.2.2 Available Potential Energy

Without dissipation, the sum of KE and available potential energy (APE) is conserved. The APE for a given scale α can be approximated by $\mathrm{APE}^{\alpha} = (B^{\alpha})^2/N^2/2$ [*Lorenz*, 1955; *Pauluis*, 2007], which is proportional to the buoyancy variance. While this formula does not hold exactly for a moist

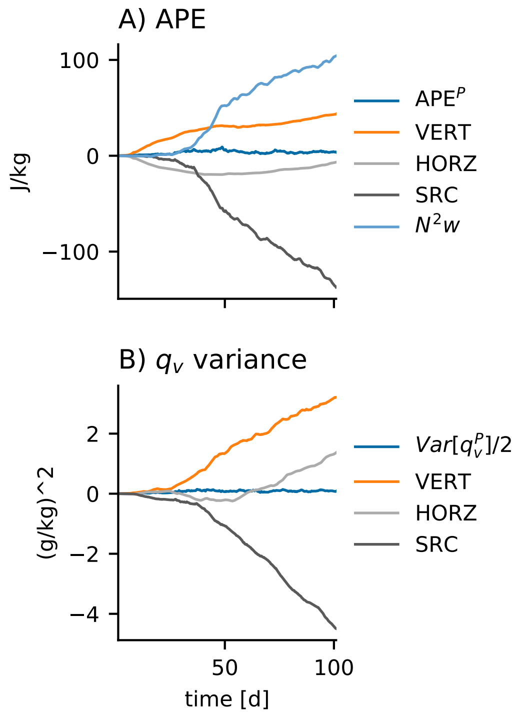

Figure 8. Mass-weighted and vertically averaged planetary-scale budgets of APE (A) and moisture variance (B). Each panel shows the cumulative effect of the feedbacks due to vertical advection (VERT), horizontal advection (HORZ), and residual source terms (SRC). Panel A also shows the APE^P is a function of time, while panel B shows moisture variance.

atmosphere, it is still useful to analyze. This approximate APE budget is given by

$$\frac{\partial \mathrm{APE}^\alpha}{\partial t} = \frac{\overline{B^\alpha H_B^\alpha}}{N^2} + \frac{\overline{B^\alpha V_B^\alpha}}{N^2} - \overline{B^\alpha w^\alpha} + \frac{\overline{B^\alpha S_B^\alpha}}{N^2}. \tag{15}$$

For simplicity, we have included smaller term $N^2 wB/g$ from Eq. 8 in the residual S_B.

The KE and APE budget exchange energy through pressure gradients and $N^2 w$ term. To see this, we must first assume hydrostatic balance holds on all the scales α, so that $\phi_z^\alpha = B^\alpha$. Then,

$$\langle \overline{B^\alpha w^\alpha} \rangle = -\langle \overline{\phi^\alpha w_z^\alpha} \rangle = -\langle \overline{\phi_x^\alpha u^\alpha} \rangle. \tag{16}$$

The first equality follows from vertical partial integration and hydrostatic balance, while the second equality follows from horizontal partial integration and the divergence free condition.

Panel A of Figure 8 shows the cumulative impact of the feedbacks in the planetary-scale APE budget. Overall, APE^P is much smaller than KE^P, which is a consequence of the weak temperature gradient observed in the tropics. The $w^\alpha B^\alpha$ feedback is the largest positive feedback, and it almost perfectly balances the pressure gradient feedback in the KE budget (cf. Figure 6B, as expected from the analysis in Eq. 16). Both vertical advection and horizontal advection play a secondary role, but are still fairly significant. The conversion of KE^P to APE^P is mostly balanced by the source terms, which include the effect of latent heating and any errors in the original budget equations. Because the radiative heating is homogeneous in space, it does not appear in the planetary-scale buoyancy or APE^P budgets. Therefore, latent heating and mixing are the dominant sinks of both APE and total energy on the planetary scale.

5.2.3 Moisture Variance

The moisture variance budget provides another perspective on the planetary-scale organization in the QSTRAT simulation. Its budget equation is given by replacing f^α with q_v^P in Eq. 12, and Figure 8B shows the cumulative effective of the feedbacks. As with the APE^P budget, the overall moisture variance is small relative to the cumulative effect of its feedbacks. The dominant positive feedback is vertical advection, which is primarily balanced by the residual source terms. Horizontal advection becomes more important around day 70, but we do not discuss this result further. The residual terms primarily consist of condensation and evaporation, so again we see moist convection damps the planetary-scale variance of this simulation. On the other hand, the positive feedback from vertical advection is mainly due to advection of the zonal mean moisture profile by the planetary-scale vertical velocity (not shown).

5.2.4 Summary

In summary, the planetary-scale vertical velocity is the primary positive feedback in both the planetary-scale moisture variance and APE budgets. On the other hand, the residual source terms, due mostly to latent heating, remove planetary-scale variance. Because w^α is proportional to the magnitude of u^α, feedbacks which increase the planetary-scale KE also would tend to increase the APE and moisture variance. Therefore, we now focus on the largest positive KE feedback, which is due to vertical advection.

6 Multiscale Interactions

6.1 Triad interactions

The most important positive feedback in both the planetary and synoptic-scale KE budget was due to vertical advection, which is a nonlinear term. As discussed at the beginning of Section 4, the multiscale theories predict that vertical eddy-flux convergences from smaller scales directly force the budgets for large-scale quantities. In this section, we use the low-pass filters introduced in Section 4 to further decompose the vertical advection terms into multiscale interactions.

We decompose vertical flux of zonal momentum into the product of different scales, so that

$$wu = \sum_{\alpha,\beta \in \{P,S,M\}} w^\alpha u^\beta.$$

Projecting this onto the target scale γ gives

$$(wu)^\gamma = \sum_{\alpha,\beta \in \{P,S,M\}} (w^\alpha u^\beta)^\gamma \tag{17}$$

In this equation, the individual $(w^\alpha u^\beta)^\gamma$ terms are known as *triad interactions* between the three scales α, β, and γ. An example triad interaction would be the planetary-scale component of the mesoscale-mesoscale interactions, which is given by $(w^M u^M)^P$.

Each of these triad interactions has a separate impact on the total vertical advection feedback for a given target scale γ. To see this, we first use partial integration to separate the total vertical advection feedback into a surface flux contribution and an internal contribution. Then, substituting Eq. 17 gives

$$\left\langle \overline{u^\gamma V_u^\gamma} \right\rangle = \overline{u^\gamma [\rho_0 u w]_{z=0}^\gamma} + \sum_{\alpha,\beta \in \{P,S,M\}} \left\langle \overline{u_z^\gamma (w^\alpha u^\beta)^\gamma} \right\rangle. \tag{18}$$

The first term on the right hand side is the mass weighted covariance of the γ-scale surface fluxes and zonal momentum. The summands in the second term quantify the impact of each vertical triad interaction on the γ-scale KE budget.

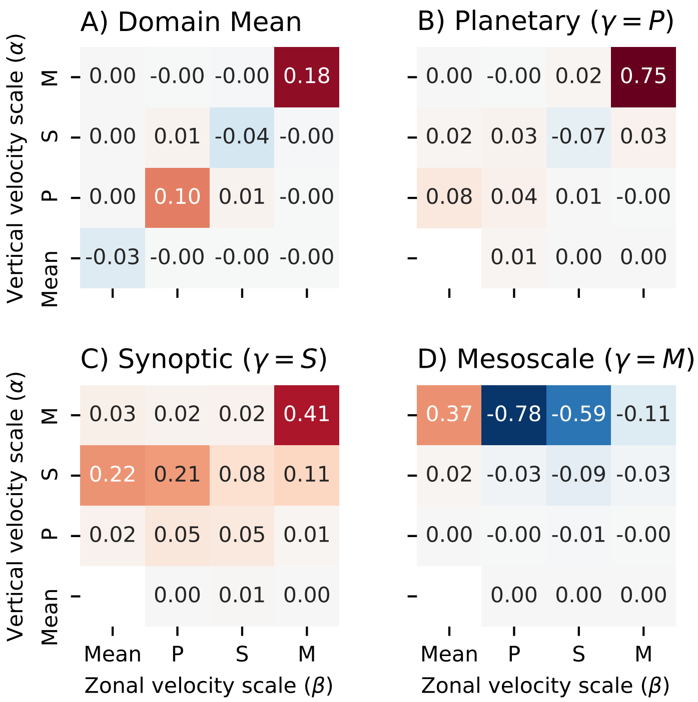

Figure 9. Decomposition of mass and time averaged kinetic energy feedbacks into triad interactions. Each number in this heat plot shows the feedback given by $\left\langle \overline{u_z^\gamma (w^\alpha u^\beta)^\gamma} \right\rangle / M$, where $M = \langle 1 \rangle$ is the mass of the atmospheric column. The units of these numbers are given in $\mathrm{J\,kg^{-1}\,d^{-1}}$. Each square is colored according to the sign and magnitude of the feedback. Dark red (blue) indicates a strong positive (negative) feedback. The four panels show the triad interactions for the target scale γ. In each panel, the horizontal axis shows the zonal velocity scale (β), and the vertical axis shows the vertical velocity target scale (α). For instance, the feedback on the planetary-scale KE budget due to advection of mesoscale zonal momentum by the mesoscale vertical velocity has a value of $0.75\,\mathrm{J\,kg^{-1}\,d^{-1}}$, and is shown in the upper right corner of panel B.

We now focus on the triad interactions terms in the right hand side of Eq. 18. We compute the time-average of $\left\langle \overline{u_z^\gamma (w^\alpha u^\beta)^\gamma} \right\rangle$ over the full 100 days for every combination of scales $\alpha, \beta, \gamma \in$ {Domain Mean, P, S, M}, and summarize the results as heat map in Figure 9. This plot also shows the triad interactions for the domain mean and mesoscale kinetic energy, two budgets which we have not discussed yet.

The most important result from Figure 9 is that flux of mesoscale zonal momentum by mesoscale vertical velocity is the strongest triad interaction in the domain mean, planetary scale, and synoptic-scale. This is clear in the planetary-scale KE budget, which we have studied extensively so far, where this term has a value of $0.75\,\mathrm{J\,kg^{-1}\,d^{-1}}$. Over the 100 d course of the simulation, this feedback will accumulate to $75\,\mathrm{J\,kg^{-1}}$, which explains most of the positive feedback due to vertical advection, which in turn is the most important positive feedback overall (cf. Figure 6). Similarly, the planetary-scale planetary-scale vertical eddy flux of zonal momentum projects strongly onto the domain-mean KE budget. This result confirms that up-scale eddy flux convergences of small-scale quantities can drive large-scale organization, as predicted by multiscale asymptotic theory [*Majda*, 2007].

The other important triad interactions are all related to advection of larger-scale zonal momentum by the γ-scale vertical velocity. These interactions are analogous to terms like $\bar{u}w'$ that appear in multiscale asymptotic theories [*Biello et al.*, 2010], and they also affect the momentum budget in a similar way to the $N^2 w$ term in the buoyancy budget (cf. Eq. 8).

Taken together, these results indicate that the projection of the vertical momentum flux onto a given scale γ can be approximated by

$$(wu)^\gamma \approx \sum_{\alpha<\gamma} (w^\alpha u^\alpha)^\gamma + \sum_{\alpha>\gamma} (w^\gamma u^\alpha)^\gamma. \tag{19}$$

The first term on the right hand side is the eddy-flux terms and the second term is the vertical advection of the larger-scale momentum by current scale's vertical velocity. These are the only two categories of advective nonlinearity that multiscale asymptotic theories allow. Thus, these results confirm that asymptotic theory can explain the multiscale organization in the QSTRAT simulation.

6.2 Eddy Transfer of Momentum, Buoyancy, and Temperature

In the previous sections, we use the KE budget to conclude that mesoscale eddy-fluxes of zonal momentum promote the planetary-scale organization seen in the QSTRAT run. While the budgets of positive definite quantities like the KE, APE, and moisture variance are useful for identifying the magnitudes of feedbacks, it is easier to interpret results in terms of the original budgets for u, B, and

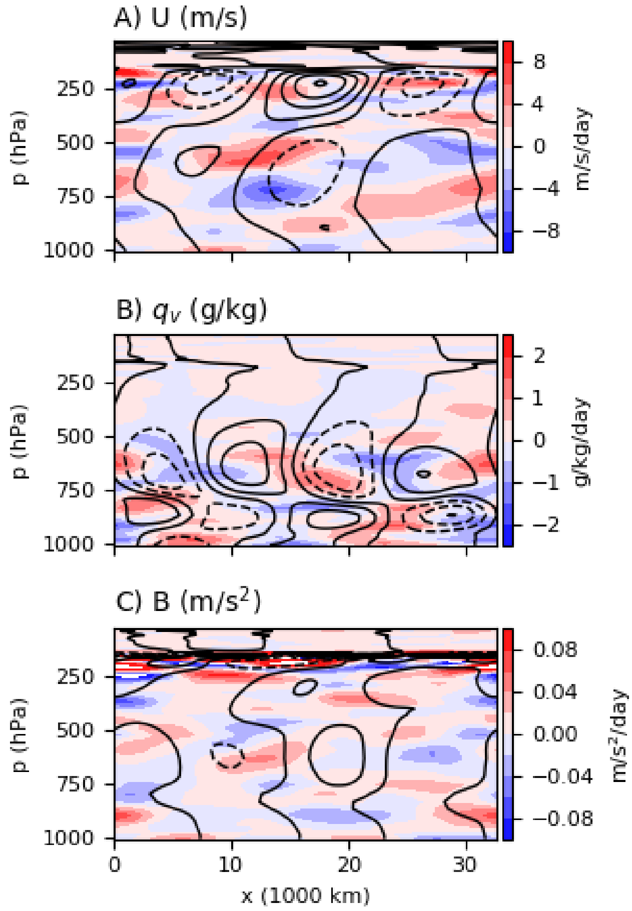

Figure 10. A cross section of planetary-scale fields and the corresponding eddy fluxes for day 85 of the QSTRAT simulation. The panels show u^P (A), q_v^P (B), and B^P (C) in contours. Negative (positive) planetary-scale anomalies are dashed (solid). The contours are spaced by $2\,\mathrm{m\,s^{-1}}$ for u, $0.5\,\mathrm{g\,kg^{-1}}$ for q_v, and $0.05\,\mathrm{m\,s^{-2}}$ for B. The corresponding eddy flux convergences $(-\frac{1}{\rho_0}(\rho_0 w' f')^P)$ from smaller scales $(f' = f^M + f^S)$ are shown in colors.

q. For instance, Equation 19 implies that the planetary-scale momentum budget can be approximated by

$$\frac{\partial u^P}{\partial t} = -\frac{1}{\rho_0}(\rho_0 u' w')_z^P - \phi_x^P + S_u^P, \tag{20}$$

where $u' = u^M + u^S$ and $w' = w^M + w^S$. The first term on the right hand side of this equation describes vertical eddy-flux terms, which play an important role it theoretical models for the multiscale organization of tropical convection.

As mentioned in the introduction, multiscale models are derived by following the multiscale asymptotic method [*Majda and Klein*, 2003; *Majda*, 2007] and are useful for understanding the interactions of tropical convection across multiple spatio-temporal scales [*Biello and Majda*, 2005; *Majda et al.*, 2010a,b; *Yang et al.*, 2017]. For example, the intraseasonal multiscale moist dynamics (IMMD) model, derived by *Biello et al.* [2010], describes the scale interactions of tropical convection from synoptic-scale to planetary/intraseasonal time scales. It also provides a multiscale framework to assess the up-scale impact of synoptic-scale waves on the MJO with a mean background flow. The mesoscale equatorial synoptic dynamics (MESD) model, derived by *Majda* [2007], is shown to be useful for modeling cloud-supercluster interactions across meso- and synoptic-scales, such as convectively coupled Kelvin waves [*Yang and Majda*, 2017, 2018a] and 2-day waves [*Yang and Majda*, 2018b].

In the IMMD model of *Biello et al.* [2010] for synoptic- and planetary-scale interactions, three eddy terms appear at the right hand side of the governing equations. They describe the up-scale impact of momentum, temperature and moisture from wave trains of synoptic-scale circulations on planetary-scale intraseasonal oscillations. Generally, the eddy term $-\frac{1}{\rho_0}(\rho_0 w' f')_z^P$ is used to account for all eddy transfer effects below the planetary scale.

Figure 10 shows the planetary-scale zonal velocity, moisture and buoyancy as well as their eddy transfer terms in a longitude-height diagram for day 85 of the QSTRAT simulation. Recall from Figure 2 that the planetary-scale wave propagates to the east. As shown by Fig.10A, the planetary-scale zonal velocity perturbation is dominated by wavenumber 1-2 and characterized by the upward/westward tilts below 500 hPa and the opposite vertical tilts above that level. This structure is frequently observed for CCEWs [*Kiladis et al.*, 2009] and the MJO [*Zhang*, 2005; *Kiladis et al.*, 2005], although the tilt in the QSTRAT run changes direction near 500 hPa, which is much shallower than in observations. The eddy transfer of zonal momentum $-\frac{1}{\rho_0}(\rho_0 w' u')_z^P$ is generally in phase with the planetary-scale circulation, and the amplitude is strongest in the regions with planetary-scale wind convergence. In these regions, the eddy-transfer is positive above 600 hPa and negative below.

Extra eddy transfer of zonal momentum is also seen near the surface and the tropopause. As for moisture in Fig.10B, most significant planetary-scale moisture anomalies are confined at levels below 400 hPa, which have upward/eastward tilts from the surface to 800 hPa and upward/westward tilts above 800 hPa. The eddy transfer of moisture $-\frac{1}{\rho_0}(\rho_0 w' q_v')_z^P$ is dominated by the second-baroclinic mode and appears to be out of phase with respect to q_v^P. In Fig.10C, the planetary-scale buoyancy is mostly upright with its maximum value in the middle troposphere at 500 hPa. The eddy transfer of buoyancy $-\frac{1}{\rho_0}(\rho_0 w' B')_z^P$ reaches its maximum strength near the tropopause at 200 hPa, but has negligible magnitude in the troposphere, except for some anomalies near the surface.

According to previous results from multiscale models for organized convection, the vertical profile of eddy transfer terms should be directly connected with the propagation direction of small-scale disturbances of tropical convection in a front-to-rear tilt. As indicated by Figure 4 of *Yang and Majda* [2018a], westward-propagating mesoscale disturbances of tropical convection tend to induce eddy transfer of zonal momentum with eastward momentum forcing above westward momentum forcing. This pattern is mainly due to the positive correlation between upward (downward) motion and westerly (easterly) winds in eddy fluxes ($w'u'$). Thus, the sign and magnitude of the eddy momentum transfer shown in Figure 10 are consistent with the westward-propagating MCSs shown in Figure 2, which *Grabowski and Moncrieff* [2001] discuss at length. Taken together with the results of Sections 5.2.1 and 6.1, this implies that eddy transfer by these MCSs dominates the total planetary-scale energy budget (i.e. $\mathrm{KE}^P + \mathrm{APE}^P$).

7 Discussion and Conclusion

Two dimensional simulations using a cloud-resolving model can spontaneously generate planetary-scale disturbance even without surface flux or radiative feedbacks. We performed three experiments in a periodic planetary-scale domain without rotation, a setup intended to model the atmosphere at the equator. The zonal mean winds are relaxed towards a barotropic $-10\,\mathrm{m\,s^{-1}}$ wind with a time-scale of 1 d. One of the simulations is run with interactive long-wave radiation and surface fluxes, while the other two are run with fixed radiation and surface fluxes. The simulation with interactive radiation and surface fluxes (LW) develops a self-aggregated planetary-scale convective structure around 80 days after initialization. On other hand, the simulation with fixed radiation and surface fluxes and stratospheric heating (QSTRAT) develops a propagating planetary-scale wave after only 30 days. The difference in these organization time scales suggests that the organizing feedbacks in the QSTRAT simulation are stronger than in the LW simulation. This planetary-scale wave has a hierarchical structure, and contains many eastward-propagating synoptic-scale waves, each of which contains many westward-propagating mesoscale convective systems (MCS). *Grabowski and Moncrieff* [2001] document these MCSs, which probably arise from interactions with imposed barotropic winds.

Based on this three-scale structure, we use low-pass filters in zonal space to decompose the model outputs into domain mean, planetary-, synoptic-, and meso-scale components. We then decompose the governing equations for zonal momentum, buoyancy, and water vapor using this strategy. From here, it is straightforward to derive variance budgets for these same quantities. These variance budgets are related to energetic quantities because the variance of momentum and buoyancy are the proportional to the planetary-scale kinetic energy (KE^P) and available potential energy (APE^P).

The budgets of KE^P, APE^P, and moisture variance quantify the strength of the feedbacks behind the planetary-scale wave in the QSTRAT simulation, and lack thereof in the simulation without stratospheric heating (Control). In the Control run, the KE sink in the stratosphere is balanced by converting potential energy to kinetic energy. The stratospheric heating in QSTRAT effectively turns the tropopause into a rigid lid by dramatically increasing the stability there. This, then, dramatically reduces the amount of dissipation occurring the stratosphere and allows the vertical advection feedbacks to dominate. The energy created by these is then converted to potential energy and ultimately damped by residual buoyancy sources.

Because the vertical advection feedback dominates the KE^P budget, we further decompose this term into the sum of many nonlinear triad interactions, and find that mesoscale vertical eddy-fluxes of momentum are the largest positive feedback in the KE^P budget. These eddy-fluxes tend to create eastward (westward) planetary-scale momentum below (above) 600 hPa, which is exactly the pattern one expects a westward-propagating MCS to produce. We therefore conclude that mesoscale organization with a consistent propagating direction is a key ingredient for planetary-scale organization generated through multiscale feedbacks.

In summary, mesoscale convective organization can induce planetary-scale convective organization even without surface flux and radiative feedbacks provided that the stratospheric dissipation is small. The idea that the stratosphere can control intraseasonal oscillation in the troposphere is not new, and our results could be linked to a recently observed relationship between the quasi-biennial oscillation (QBO) in the stratosphere and of Madden-Julian oscillation (MJO) [*Yoo and Son*, 2016]. While the simulations in this paper are simplistic by design, the diagnostic framework we use could help identify the important feedback processes in the real MJO. In particular, future studies could quantify the relative importance of surface flux, radiative, and multiscale feedbacks in observations or more realistic models.

Acknowledgments

N.B. is supported as a postdoctoral fellow by the Washington Research Foundation, and by a Data Science Environments project award from the Gordon and Betty Moore Foundation (Award #2013-10-29) and the Alfred P. Sloan Foundation (Award #3835) to the University of Washington eScience Institute. The research of A.J.M. is partially supported by the Office of Naval Research ONR MURI N00014-12-1-0912 and the Center for Prototype Climate Modeling (CPCM) in the New York University Abu Dhabi (NYUAD) Research Institute. Q.Y. is funded as a postdoctoral fellow by CPCM in the NYUAD Research Institute. Due to size limitations, the model outputs are archived on UW and NYU servers and can be obtained via e-mail request to the first author.

References

Aluie, H., M. Hecht, and G. K. Vallis (2017), Mapping the energy cascade in the north atlantic ocean: The Coarse-Graining approach, *J. Phys. Oceanogr.*, *48*(2), 225–244, doi:10.1175/JPO-D-17-0100.1.

Biello, J. A., and A. J. Majda (2005), A new multiscale model for the madden–julian oscillation, *Journal of the atmospheric sciences*, *62*(6), 1694–1721.

Biello, J. A., and A. J. Majda (2006), Modulating synoptic scale convective activity and boundary layer dissipation in the ipesd models of the madden–julian oscillation, *Dynamics of atmospheres and oceans*, *42*(1-4), 152–215.

Biello, J. A., A. J. Majda, et al. (2010), Intraseasonal multi-scale moist dynamics of the tropical atmosphere, *Communications in Mathematical Sciences*, *8*(2), 519–540.

Bretherton, C. S., and M. F. Khairoutdinov (2015), Convective self-aggregation feedbacks in near-global cloud-resolving simulations of an aquaplanet, *Journal of Advances in Modeling Earth Systems*, *7*(4), 1765–1787.

Bretherton, C. S., P. N. Blossey, and M. Khairoutdinov (2005), An Energy-Balance analysis of deep convective Self-Aggregation above uniform SST, *J. Atmos. Sci.*, *62*(12), 4273–4292, doi:10.1175/JAS3614.1.

Chen, S. S., R. A. Houze Jr, and B. E. Mapes (1996), Multiscale variability of deep convection in realation to large-scale circulation in toga coare, *Journal of the Atmospheric Sciences*, *53*(10), 1380–1409.

Goswami, B. B., B. Khouider, R. Phani, P. Mukhopadhyay, and A. J. Majda (2017a), Improved tropical modes of variability in the NCEP climate forecast system (version 2) via a stochastic multicloud model, *J. Atmos. Sci.*, *74*(10), 3339–3366, doi:10.1175/JAS-D-17-0113.1.

Goswami, B. B., B. Khouider, R. Phani, P. Mukhopadhyay, and A. Majda (2017b), Improving synoptic and intraseasonal variability in CFSv2 via stochastic representation of organized convection: CFSsmcm, *Geophys. Res. Lett.*, *44*(2), 1104–1113, doi:10.1002/2016GL071542.

Grabowski, W. W., and M. W. Moncrieff (2001), Large-scale organization of tropical convection in two-dimensional explicit numerical simulations, *Quarterly Journal of the Royal Meteorological Society*, *127*(572), 445–468.

Held, I. M., R. S. Hemler, and V. Ramaswamy (1993), Radiative-Convective equilibrium with explicit Two-Dimensional moist convection, *J. Atmos. Sci.*, *50*(23), 3909–3927, doi:10.1175/1520-0469(1993)050<3909:RCEWET>2.0.CO;2.

Houze, R. A. (2004), Mesoscale convective systems, *Reviews of Geophysics*, *42*(4).

Johnson, R. H., T. M. Rickenbach, S. A. Rutledge, P. E. Ciesielski, and W. H. Schubert (1999), Trimodal characteristics of tropical convection, *Journal of climate*, *12*(8), 2397–2418.

Khain, A., K. Beheng, A. Heymsfield, A. Korolev, S. Krichak, Z. Levin, M. Pinsky, V. Phillips, T. Prabhakaran, A. Teller, et al. (2015), Representation of microphysical processes in cloud-resolving models: Spectral (bin) microphysics versus bulk parameterization, *Reviews of Geophysics*, *53*(2), 247–322.

Khairoutdinov, M., and K. Emanuel (2013), Rotating radiative-convective equilibrium simulated by a cloud-resolving model, *Journal of Advances in Modeling Earth Systems*, *5*(4), 816–825.

Khairoutdinov, M. F., and D. A. Randall (2003), Cloud resolving modeling of the arm summer 1997 iop: Model formulation, results, uncertainties, and sensitivities, *Journal of the Atmospheric Sciences*, *60*(4), 607–625.

Khouider, B., and A. J. Majda (2006), Multicloud convective parametrizations with crude vertical structure, *Theoretical and Computational Fluid Dynamics*, *20*(5-6), 351–375.

Khouider, B., and A. J. Majda (2008), Multicloud models for organized tropical convection: Enhanced congestus heating, *Journal of the Atmospheric Sciences*, *65*(3), 895–914.

Kiladis, G. N., K. H. Straub, and P. T. Haertel (2005), Zonal and vertical structure of the madden–julian oscillation, *Journal of the atmospheric sciences*, *62*(8), 2790–2809.

Kiladis, G. N., M. C. Wheeler, P. T. Haertel, K. H. Straub, and P. E. Roundy (2009), Convectively coupled equatorial waves, *Reviews of Geophysics*, *47*(2).

Lorenz, E. N. (1955), Available potential energy and the maintenance of the general circulation, *Tell'Us*, *7*(2), 157–167, doi:10.1111/j.2153-3490.1955.tb01148.x.

Madden, R. A., and P. R. Julian (1971), Detection of a 40–50 day oscillation in the zonal wind in the tropical pacific, *Journal of the atmospheric sciences*, *28*(5), 702–708.

Madden, R. A., and P. R. Julian (1972), Description of global-scale circulation cells in the tropics with a 40–50 day period, *Journal of the atmospheric sciences*, *29*(6), 1109–1123.

Majda, A. J. (2007), New multiscale models and self-similarity in tropical convection, *Journal of the atmospheric sciences*, *64*(4), 1393–1404.

Majda, A. J., and J. A. Biello (2004), A multiscale model for tropical intraseasonal oscillations, *Proceedings of the National Academy of Sciences of the United States of America*, *101*(14), 4736–4741.

Majda, A. J., and R. Klein (2003), Systematic multiscale models for the tropics, *Journal of the Atmospheric Sciences*, *60*(2), 393–408.

Majda, A. J., and S. N. Stechmann (2009), The skeleton of tropical intraseasonal oscillations, *Proceedings of the National Academy of Sciences*, *106*(21), 8417–8422.

Majda, A. J., and Q. Yang (2016), A multiscale model for the intraseasonal impact of the diurnal cycle over the maritime continent on the madden–julian oscillation, *Journal of the Atmospheric Sciences*, *73*(2), 579–604.

Majda, A. J., Y. Xing, et al. (2010a), New multi-scale models on mesoscales and squall lines, *Communications in Mathematical Sciences*, *8*(1), 113–134.

Majda, A. J., Y. Xing, and M. Mohammadian (2010b), Moist multi-scale models for the hurricane embryo, *Journal of Fluid Mechanics*, *657*, 478–501.

Mapes, B., S. Tulich, J. Lin, and P. Zuidema (2006), The mesoscale convection life cycle: Building block or prototype for large-scale tropical waves?, *Dynamics of atmospheres and oceans*, *42*(1-4), 3–29.

Moncrieff, M. W., C. Liu, and P. Bogenschutz (2017), Simulation, modeling, and dynamically based parameterization of organized tropical convection for global climate models, *Journal of the Atmospheric Sciences*, *74*(5), 1363–1380.

Muller, C. J., and I. M. Held (2012), Detailed investigation of the Self-Aggregation of convection in Cloud-Resolving simulations, *J. Atmos. Sci.*, *69*(8), 2551–2565, doi:10.1175/JAS-D-11-0257.1.

Nakazawa, T. (1988), Tropical super clusters within intraseasonal variations over the western pacific, *Journal of the Meteorological Society of Japan. Ser. II*, *66*(6), 823–839.

Pauluis, O. (2007), Sources and sinks of available potential energy in a moist atmosphere, *J. Atmos. Sci.*, *64*(7), 2627–2641, doi:10.1175/JAS3937.1.

Pauluis, O. (2008), Thermodynamic consistency of the anelastic approximation for a moist atmosphere, *J. Atmos. Sci.*, *65*(8), 2719–2729, doi:10.1175/2007JAS2475.1.

Prein, A. F., W. Langhans, G. Fosser, A. Ferrone, N. Ban, K. Goergen, M. Keller, M. Tölle, O. Gutjahr, F. Feser, et al. (2015), A review on regional convection-permitting climate modeling: Demonstrations, prospects, and challenges, *Reviews of geophysics*, *53*(2), 323–361.

Slawinska, J., O. Pauluis, A. J. Majda, and W. W. Grabowski (2014), Multiscale interactions in an idealized walker circulation: Mean circulation and intraseasonal variability, *Journal of the Atmospheric Sciences*, *71*(3), 953–971.

Wheeler, M., and G. N. Kiladis (1999), Convectively coupled equatorial waves: Analysis of clouds and temperature in the wavenumber-frequency domain, *J. Atmos. Sci.*, *56*(3), 374–399.

Wing, A. A., and T. W. Cronin (2016), Self-aggregation of convection in long channel geometry: Self-Aggregation in channel geometry, *Quart. J. Roy. Meteor. Soc.*, *142*(694), 1–15, doi:10.1002/qj.2628.

Wing, A. A., and K. A. Emanuel (2014), Physical mechanisms controlling self-aggregation of convection in idealized numerical modeling simulations, *J. Adv. Model. Earth Syst.*, *6*(1), 59–74, doi:10.1002/2013MS000269.

Yang, D. (2017), Boundary layer height and buoyancy determine the horizontal scale of convective Self-Aggregation, *J. Atmos. Sci.*, *75*(2), 469–478, doi:10.1175/JAS-D-17-0150.1.

Yang, Q., and A. J. Majda (2014), A multi-scale model for the intraseasonal impact of the diurnal cycle of tropical convection, *Theoretical and Computational Fluid Dynamics*, *28*(6), 605–633.

Yang, Q., and A. J. Majda (2017), Upscale impact of mesoscale disturbances of tropical convection on synoptic-scale equatorial waves in two-dimensional flows, *Journal of the Atmospheric Sciences*, *74*(9), 3099–3120.

Yang, Q., and A. J. Majda (2018a), Upscale impact of mesoscale disturbances of tropical convection on convectively coupled kelvin waves, *Journal of the Atmospheric Sciences*, *75*(1), 85–111.

Yang, Q., and A. J. Majda (2018b), Upscale impact of mesoscale disturbances of tropical convection on 2-day waves, *submitted to Journal of the Atmospheric Sciences*.

Yang, Q., A. J. Majda, and B. Khouider (2017), Itcz breakdown and its upscale impact on the planetary-scale circulation over the eastern pacific, *Journal of the Atmospheric Sciences*, *74*(12), 4023–4045.

Yoo, C., and S.-W. Son (2016), Modulation of the boreal wintertime Madden-Julian oscillation by the stratospheric quasi-biennial oscillation, *Geophys. Res. Lett.*, *43*(3), 2016GL067,762, doi: 10.1002/2016GL067762.

Zhang, C. (2005), Madden-julian oscillation, *Reviews of Geophysics*, *43*(2).